

TIME-INDEPENDENT SPIKING NEURON VIA MEMBRANE POTENTIAL ESTIMATION FOR EFFICIENT SPIKING NEURAL NETWORKS

Hanqi Chen¹, Lixing Yu^{1*}, Shaojie Zhan¹, Penghui Yao¹, Jiankun Shao²

¹School of Information Science and Engineering, Yunnan University, Yunnan, China

²State Key Laboratory of Explosion Science and Technology, Beijing Institute of Technology, Beijing, China

ABSTRACT

The computational inefficiency of spiking neural networks (SNNs) is primarily due to the sequential updates of membrane potential, which becomes more pronounced during extended encoding periods compared to artificial neural networks (ANNs). This highlights the need to parallelize SNN computations effectively to leverage available hardware parallelism. To address this, we propose Membrane Potential Estimation Parallel Spiking Neurons (MPE-PSN), a parallel computation method for spiking neurons that enhances computational efficiency by enabling parallel processing while preserving the intrinsic dynamic characteristics of SNNs. Our approach exhibits promise for enhancing computational efficiency, particularly under conditions of elevated neuron density. Empirical experiments demonstrate that our method achieves state-of-the-art (SOTA) accuracy and efficiency on neuromorphic datasets without requiring additional training parameters. Codes are available at <https://github.com/chratzee/MPE-PSN>.

Index Terms— Parallel Spiking Neurons, Membrane Potential Estimation, Efficient Computing

1. INTRODUCTION

At the heart of spiking neural networks (SNNs) lie dynamic spiking neurons, intricately handling inputs, revealing intricate neuronal dynamics, and triggering spikes upon membrane potential thresholds being surpassed. While spiking neurons currently operate with sequential computational updates, their energy efficiency coexists with computational inefficiency, leading to latency issues in training and inference compared to artificial neural networks (ANNs).

Prior advancements in spiking neurons, such as PLIF [1] integrating a learnable time constant, IM-LIF [2] incorporating attention mechanisms, GLIF [3] featuring gating mechanisms, and KLIF [4] optimizing activation slopes and surrogate gradient curve width, have predominantly operated within a sequential computational framework. This underscores the need for exploring parallelized computation approaches leveraging the potential of spiking neurons.

* Corresponding author.

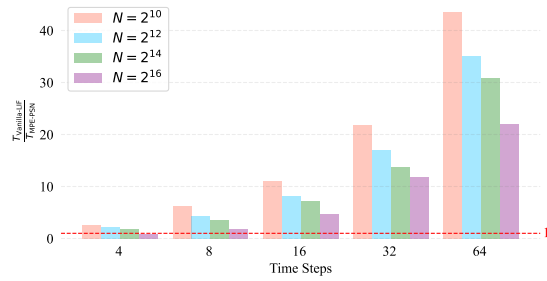


Fig. 1. Variations in the execution time ratio between the vanilla LIF neuron and the MPE-PSN neuron concerning time step increments and neuron quantity augmentation in both cases during the forward process, denoted as $\frac{T_{\text{vanilla LIF}}}{T_{\text{MPE-PSN}}}$.

Research by Parallel Spiking Neurons (PSN) [5] introduces a parallelized spiking neuron design by circumventing the reset process inherent in SNNs. However, this approach compromises the distinctive high dynamic properties of spiking neurons, causing the operational mechanism of SNNs to mirror that of ANNs instead. And Parallel Multi-compartment Spiking Neuron (PMSN) [6] elevates neuronal dynamics and enables the parallelization of dynamic neuronal computations, albeit maintaining temporal dependence.

To address prevailing challenges, we introduce a Membrane Potential Estimation Parallel Spiking Neuron (MPE-PSN), a highly dynamic and fully parallelized computational neuron. MPE-PSN estimates the activation output through the spiking probability of the membrane potential, thereby decoupling spiking neuron computations from temporal dependencies. This strategy promises a substantial boost in the computational efficiency of long-temporal dependent spiking neural networks, exemplified by [7]. Throughout SNN training, the alignment between true and estimated membrane potentials is optimized using the minimum mean square error (MSE) loss function. Empirical findings validate the marked improvement in computational efficiency offered by the proposed methodology, while preserving the intricate dynamic attributes of spiking neurons. Noteworthy performance benchmarks are attained on neuromorphic datasets.

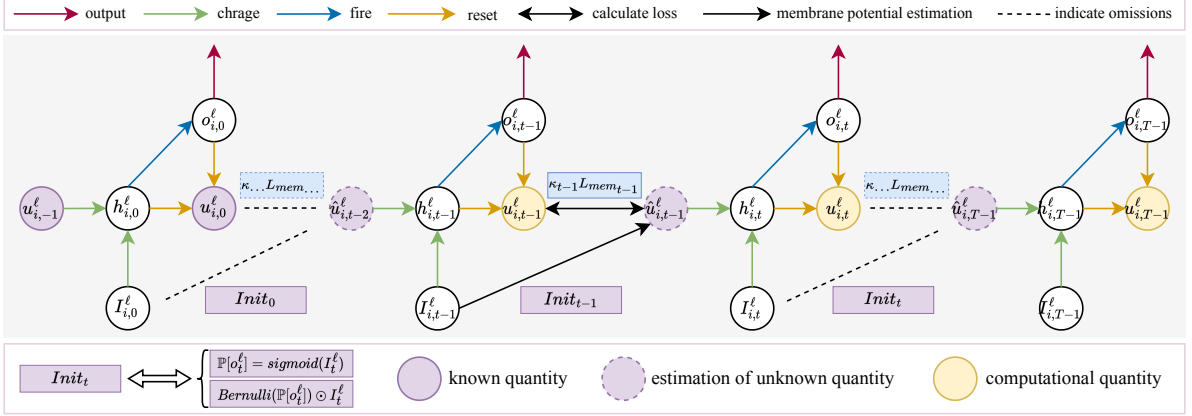


Fig. 2. Schematic diagram of the proposed neuron internal structure based on membrane potential estimation.

2. METHODS

2.1. Motivation and Derivation of Neuron Design

Spiking neurons excel in temporal information processing. Their iterative computational process can be outlined as follows:

$$h_{i,t}^l = g(u_{i,t-1}^l, I_{i,t}^l), \quad (1)$$

$$o_{i,t}^l = \Theta(h_{i,t}^l - v_{th}) = \begin{cases} 1, & u_{i,t}^l \geq v_{th}, \\ 0, & \text{otherwise,} \end{cases} \quad (2)$$

$$u_{i,t}^l = h_{i,t}^l \cdot (1 - o_{i,t}^l) + v_r \cdot o_{i,t}^l, \quad (3)$$

where $I_{i,t}^l$ denotes the input current of the i -th neuron in the l -th layer at timestep t , $u_{i,t}^l$ represents the membrane potential post-spike firing and reset, and $h_{i,t}^l$ signifies the integrated membrane potential prior to firing. The threshold for membrane potential is denoted as v_{th} , and $o_{i,t}^l$ represents the output following spike firing. The function $g(\cdot)$ in Equation (1) corresponds to distinct spiking neurons, while $\Theta(\cdot)$ in Equation (2) signifies the Heaviside step function. In Equation (3), v_r stands for the reset potential. This equation elucidates a hard reset scenario in a spiking neuron, where the membrane potential is reset from $u_{i,t}^l$ to v_r upon firing. In surrogate training, the hard reset method is favored over the soft reset approach for enhanced performance [8].

By extending the Equations (1) to (3) to Leaky Integrate-and-Fire (LIF) neuron, we obtain the Equation (4) as:

$$u_{i,t}^l = (\tau_m u_{i,t-1}^l + I_{i,t}^l)(1 - \Theta(\tau_m u_{i,t-1}^l + I_{i,t}^l, v_{th})), \quad (4)$$

where τ_m represents the membrane potential constant, input decay is disregarded, and v_r is set to 0 in this work, the iterative update of a spiking neuron adheres to a sequential, incremental process. At time step t , the output is contingent on the preceding time step $t-1$. The computational time complexity of the neuron at this stage is $\mathcal{O}(T)$, with T denoting the total number of time steps. Given the assumption

of independence of membrane potential updates from the previous time point's output, spiking neuron updates can be architected for parallel processing.

Apparently, when $t = 0$, the previous time point's membrane potential of the neuron is noted as 0, $u_{i,-1}^l = 0$. Consequently, the computation for $u_{i,0}^l$ is exact. Referring to Equation 4, we obtain:

$$u_{i,0}^l = I_{i,0}^l(1 - \Theta(I_{i,0}^l, v_{th})), \quad (5)$$

Subsequently, we initialize the estimated values of $u_{i,1}^l$, referred to as $\hat{u}_{i,1}^l$, to the estimated values of $u_{i,T-1}^l$, denoted as $\hat{u}_{i,T-1}^l$, which is determined by $I_{i,T-1}^l$, calculated as:

$$I_{i,t}^l = \sum_{j=1}^{N_{l-1}} w_{i,j}^{\ell-1} o_{j,t-1}^{\ell-1}, \quad (6)$$

Here, $w_{i,j}^{\ell-1}$ represents the synaptic weight between the j -th neuron in the preceding layer and the i -th neuron in the subsequent layer. N_{l-1} signifies the number of neurons in the $(l-1)$ -th layer.

The accurate $u_{i,0}^l$ is utilized to rectify the error, denoted as \mathcal{E} . The process unfolds as follows:

$$u_{i,t}^l = (\tau_m \hat{u}_{i,t-1}^l + I_{i,t}^l)(1 - \Theta(\tau_m \hat{u}_{i,t-1}^l + I_{i,t}^l, v_{th})), \quad (7)$$

$$u_{i,t+1}^l = (\tau_m \hat{u}_{i,t}^l + I_{i,t+1}^l)(1 - \Theta(\tau_m \hat{u}_{i,t}^l + I_{i,t+1}^l, v_{th})), \quad (8)$$

$$\mathcal{E} = \text{error}(\hat{u}_{i,t}^l, u_{i,t}^l). \quad (9)$$

The comprehensive illustration of the entire process is shown in Fig. 2.

2.2. Initialization of Estimated Membrane Potential

The output of spiking neurons, denoted by the tensor $\mathbf{o} \in \mathbb{R}^{T \times C \times H \times W}$, with T , C , H , and W representing time

Table 1. Training specifics and network architectures for diverse datasets. SGD: Stochastic Gradient Descent. C: Channel. MP: Max Pooling. AP: Average Pooling. FC: Fully Connected.

Dataset	Learning rate	Optimizer	Batch size	Epoch	Resolution	Network structure
DVSGesture	0.05	SGD	8	230	64 × 64	5 × (256C3-MP2)-FC-FC-AP
CIFAR10-DVS	0.05	SGD	32	230	48 × 48	64C3-128C3-AP2-256C3-256C3-AP2-512C3-512C3-AP2-512C3-512C3-AP2-FC
N-Caltech 101	0.01	SGD	8	230	128 × 128	64C3-128C3-AP2-256C3-256C3-AP2-512C3-512C3-AP2-512C3-512C3-AP2-FC
CIFAR10/100	0.1	Adam [10]	64	300	32 × 32	512C3-512C3-AP2-512C3-512C3-AP2-FC ResNet19 [11]

step, channel, height, and width respectively, adheres to the following distribution:

$$\mathbf{o} \sim \mathcal{N}(p, p(1-p)), \text{ i.e. } Bernoulli(), \mathbf{o} \in \{0, 1\} \quad (10)$$

The output characteristics of individual spiking neurons adhere to a *Bernoulli* distribution, where p and $1-p$ represent the probabilities of 1 and 0, respectively. Activated neurons produce spikes, while silent neurons do not. Spike generation is influenced by the input current magnitude, with neurons receiving stronger input currents having a higher likelihood of generating spikes. As outlined in [9], this can be described as:

$$\mathbf{o} \sim Bernoulli(\mathbb{P}[o_{i,t}^\ell = 1]), \quad (11)$$

Here, $\mathbb{P}[o_{i,t}^\ell = 1] = F_\epsilon(\cdot)$, where $F_\epsilon(\cdot)$ denotes the cumulative distribution function of the input current \mathbf{I} in this context, and $\mathbb{P}[\cdot]$ signifies probability.

In our study, we employ the *sigmoid* function as the $F_\epsilon(\cdot)$, utilized for evaluating the firing probabilities of each neuron.

$$\mathbb{P}[\mathbf{o}] = sigmoid(\mathbf{I}), \mathbf{I} \in \mathbb{R}^{T \times C \times H \times W} \quad (12)$$

$$\hat{\mathbf{u}} = (1 - Bernoulli(\mathbb{P}[\mathbf{o}])) \odot \mathbf{I}. \quad (13)$$

Here, the symbol \odot represents the Hadamard product. The time complexity for computing $\mathbb{P}[\mathbf{o}]$ is theoretically $O(1)$, similar to the *Bernoulli* operator. As a result, the extra time needed for this operation is negligible, especially on graphics processing unit (GPU) devices.

2.3. Membrane Potential Approximation Loss

We have addressed the discrepancy between the probabilistically initialized estimate, $\hat{u}_{i,t}^\ell$, and the computationally obtained value $u_{i,t}^\ell$ by applying a correction mechanism (i.e., in Section 2.1). Such disparity is mitigated through the utilization of the minimum mean square error (MSE) loss function to approximate the true and probabilistically initialized values. Crucially, only $u_{i,0}^\ell$ signifies the precise calculated arrival. Efficient approximation of both $\hat{u}_{i,t}^\ell$ and $u_{i,t}^\ell$ necessitates weighting different moments with distinct learnable coefficients κ_i . It formalizes the expression of \mathcal{L}_{mem} as outlined:

$$\mathcal{L}_{mem} = \sum_{t=0}^{T-1} \sum_{i=0}^{N_t-1} \kappa_i MSE(\hat{u}_{i,t}^\ell, u_{i,t}^\ell), \quad (14)$$

Conclusively, the overall loss is calculated as:

$$\mathcal{L}_{total} = (1 - \lambda) \mathcal{L}_{cls} + \lambda \mathcal{L}_{mem}, \quad (15)$$

where λ serves as a coefficient, set to 0.01. \mathcal{L}_{cls} denotes the classification loss, which is computed employing the methodology outlined in the [12]. \mathbf{o}_t and \mathbf{y} represent outputs and labels, respectively. The loss function of \mathcal{L}_{cls} is:

$$\mathcal{L}_{cls} = \frac{1}{T} \sum_{t=0}^{T-1} \mathcal{L}_{CE}[\mathbf{o}_t, \mathbf{y}]. \quad (16)$$

3. EXPERIMENTS

In direct training scenarios, the gradient is computed using the spatio-temporal backpropagation (STBP) [13] algorithm, as articulated:

$$\frac{\partial L}{\partial w_{i,j}^\ell} = \sum_{t=1}^T \frac{\partial L}{\partial o_{i,t}^\ell} \frac{\partial o_{i,t}^\ell}{\partial u_{i,t}^\ell} \frac{\partial u_{i,t}^\ell}{\partial I_{i,t}^\ell} \frac{\partial I_{i,t}^\ell}{\partial w_{i,j}^\ell}, \quad (17)$$

where $\frac{\partial o_{i,t}^\ell}{\partial u_{i,t}^\ell}$ are non-differentiable, and gradients are typically approximated using integrable functions that share similar shapes. In our study, a triangular function [12] is utilized for gradient approximation, represented mathematically as:

$$\frac{\partial o_{i,t}^\ell}{\partial u_{i,t}^\ell} = \frac{1}{\alpha^2} max(0, \alpha - |u_{i,t}^\ell - v_{th}|). \quad (18)$$

here, α serves as a constant that restricts the range of activated gradients, fixed at 1.0. The hyper-parameter configurations and network architecture details are outlined in Table 1. Additionally, τ_m is set to 0.25, with the threshold represented as a parameter subject to learning.

3.1. Comparisons With Existing Methods

We evaluated the MPE-PSN neuron in SNNs across both neuromorphic and static datasets, with the experimental results presented in Table 2.

DVSGesture [14]. We performed extensive classification experiments on the DVSGesture dataset using the 7B-Net architecture. Our methodology achieved a top-1 accuracy of 97.92% at 16 time steps. This outcome surpassed the SOTA result with 4 fewer time steps.

CIFAR10DVS [17]. We assessed the effectiveness of our method on the CIFAR10DVS dataset across time steps of 8, 10, and 16. Our results consistently outperform those of the current SOTA methods.

N-Caltech 101 [18]. Our method's efficacy was further confirmed on the N-Caltech 101 dataset, with the performance of other methods reproduced for comparison. The outcomes revealed that our approach achieved the highest accuracy presently attainable on the N-Caltech 101 dataset.

Table 2. Compare with previous studies on neuromorphic and static datasets. T represents time-steps, while B indicates learnable blocks. Prefix M signifies the term modified. Results marked with * denote self-implemented findings. The threshold parameter for Vanilla LIF and PLIF is established at 1.0 for the N-Caltech 101 dataset.

Dataset	Approach	Network	T	Accuracy(%)
DVS-Gesture	KLIF [4]	M-PLIF-Net	12	94.1
	MLF [15]	ResNet-20	40	97.29
	IM-LIF [2]	ResNet-19	40	97.33
	PLIF [1]	7B-Net	20	97.57
	MPE-PSN	7B-Net	16	97.92
CIFAR10-DVS	GLIF [3]	7B-wideNet	16	78.1
	IM-LIF [2]	VGGSN	10	80.5
	TET [12]	VGGSN	10	83.17
	SPSN [5]	VGGSN	4.8,10	82.3,85.3,85.9
	MPE-PSN	VGGSN	4.8,10	84.48,86.09,86.69
N-Caltech 101	Vanilla LIF	VGGSN	10	87.13*
	PLIF [1]	VGGSN	10	74.5*
	Mask-PSN [5]	VGGSN	10	85.78*
	MPE-PSN	VGGSN	10	88.24
CIFAR 10	KLIF [4]	M-PLIF-Net	10	92.52
	PLIF [1]	PLIF Net	8	93.50
	IM-LIF [2]	ResNet-19	6	95.66
	PSN [5]	M-PLIF-Net	4	95.32
	MPE-PSN	ResNet-19	4	94.36
CIFAR 100	TET [12]	ResNet-19	6	74.72
	TEBN [16]	ResNet-19	6	76.41
	IM-LIF [2]	ResNet-19	6	77.42
	MPE-PSN	ResNet-19	4	75.9

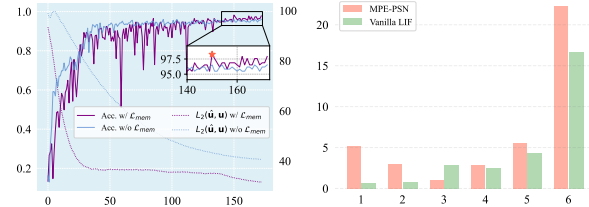
CIFAR10 & CIFAR100 [19]. Our method achieved top-1 accuracy rates of 94.36% and 75.9% on the CIFAR10 and CIFAR100 static datasets, respectively. It is important to note that the performance of our method on static datasets is not exceptional due to the high homogeneity of the data caused by directly stacking images to simulate time steps, which leads to inaccurate probabilistic estimates and, consequently, affects performance.

3.2. Membrane Potential Approximation Analysis

We also make evaluation on the accuracy of the network model with and without \mathcal{L}_{mem} and the impact of this loss on the L_2 norm of membrane potential distances. In Fig. 3 (a), for the network with \mathcal{L}_{mem} , initial epochs exhibit lower classification accuracy compared to the model without \mathcal{L}_{mem} as the network emphasizes approximating membrane potential distances. Over epochs, the \mathcal{L}_{mem} -included model achieves superior accuracy, consistently maintaining a smaller L_2 norm of membrane potential distances than the model without \mathcal{L}_{mem} .

3.3. Computational Efficiency Analysis

A comparative analysis is conducted to assess the computational speed difference between our proposed neuron model and



(a) L_2 norm($\hat{\mathbf{u}}, \mathbf{u}$) and Accuracy (b) Spike rate (%)

Fig. 3. (a): The curves of L_2 norm between $\hat{\mathbf{u}}$ and \mathbf{u} , as well as the accuracy curves on the DVSGesture dataset. The values are normalized to a range of 0 to 1. (b): Spike rate of MPE-PSN neurons and vanilla LIF neurons on the DVSGesture dataset.

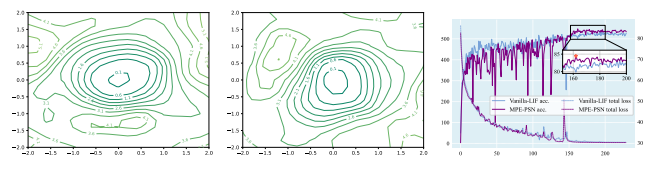


Fig. 4. 2D loss contour [20] as well as accuracy and loss curve on CIFAR10DVS dataset when time steps is 4.

the traditional LIF neuron across various time steps and neuron quantities. As depicted in Fig. 1, our neurons generally outpace vanilla LIF neurons in simulation speed. Furthermore, as shown in Fig. 3 (b), our proposed neuron exhibits a notably higher spike rate across most layers when utilizing probabilistic estimation, contrasting with the dynamic complexity observed in the vanilla LIF neuron. Fig. 4 (a) and 4 (b) illustrate that the loss contours of our proposed neurons are comparable to those of vanilla LIF neurons, with both displaying relatively flat profiles. Fig. 3 (a) and 4 (c) demonstrate that initial uncertainties in membrane potential estimation did impact the network's fitting performance. However, as the estimation of membrane potential improved, this effect became less pronounced. Consequently, our proposed neurons maintain both computational efficiency and performance integrity.

4. CONCLUSION

In this study, we introduce a parallel spiking neuron model centered on membrane potential estimation. This model enables computational parallelization while preserving neuronal dynamics, thereby notably improving the computational efficiency of spiking neural networks. Our neuron model has exhibited exceptional performance on neuromorphic datasets, pointing towards its capacity to drive the evolution of parallelized neurons in the future.

5. REFERENCES

- [1] Wei Fang, Zhaofei Yu, Yanqi Chen, Timothée Masquelier, Tiejun Huang, and Yonghong Tian, “Incorporating learnable membrane time constant to enhance learning of spiking neural networks,” in *2021 IEEE/CVF International Conference on Computer Vision (ICCV)*, 2021, pp. 2641–2651.
- [2] Shuang Lian, Jiangrong Shen, Ziming Wang, and Huajin Tang, “Im-lif: Improved neuronal dynamics with attention mechanism for direct training deep spiking neural network,” *IEEE Transactions on Emerging Topics in Computational Intelligence*, vol. 8, no. 2, pp. 2075–2085, 2024.
- [3] Xingting Yao, Fanrong Li, Zitao Mo, and Jian Cheng, “Glif: A unified gated leaky integrate-and-fire neuron for spiking neural networks,” in *Advances in Neural Information Processing Systems*, S. Koyejo, S. Mohamed, A. Agarwal, D. Belgrave, K. Cho, and A. Oh, Eds. 2022, vol. 35, pp. 32160–32171, Curran Associates, Inc.
- [4] Chunming Jiang and Yilei Zhang, “Klf: An optimized spiking neuron unit for tuning surrogate gradient slope and membrane potential,” *ArXiv*, vol. abs/2302.09238, 2023.
- [5] Wei Fang, Zhaofei Yu, Zhaokun Zhou, Ding Chen, Yanqi Chen, Zhengyu Ma, Timothée Masquelier, and Yonghong Tian, “Parallel spiking neurons with high efficiency and ability to learn long-term dependencies,” in *Advances in Neural Information Processing Systems*, A. Oh, T. Naumann, A. Globerson, K. Saenko, M. Hardt, and S. Levine, Eds. 2023, vol. 36, pp. 53674–53687, Curran Associates, Inc.
- [6] Xinyi Chen, Jibin Wu, Chenxiang Ma, Yinsong Yan, and KC Tan, “A parallel multi-compartment spiking neuron for multi-scale sequential modeling,” 2024.
- [7] Lixing Yu, Hanqi Chen, Ziming Wang, Shaojie Zhan, Jiankun Shao, Qingjie Liu, and Shu Xu, “Spikingvit: a multi-scale spiking vision transformer model for event-based object detection,” *IEEE Transactions on Cognitive and Developmental Systems*, pp. 1–17, 2024.
- [8] Eimantas Ledinauskas, Julius Ruseckas, Alfonsas Jursenas, and Giedrius Burachas, “Training deep spiking neural networks,” *ArXiv*, vol. abs/2006.04436, 2020.
- [9] Gehua Ma, Rui Yan, and Huajin Tang, “Exploiting noise as a resource for computation and learning in spiking neural networks,” *Patterns*, vol. 4, no. 10, pp. 100831, 2023.
- [10] Diederik P. Kingma and Jimmy Ba, “Adam: A method for stochastic optimization,” 2017.
- [11] Kaiming He, Xiangyu Zhang, Shaoqing Ren, and Jian Sun, “Deep residual learning for image recognition,” in *2016 IEEE Conference on Computer Vision and Pattern Recognition (CVPR)*, 2016, pp. 770–778.
- [12] Shikuang Deng, Yuhang Li, Shanghang Zhang, and Shi Gu, “Temporal efficient training of spiking neural network via gradient re-weighting,” in *International Conference on Learning Representations*, 2022.
- [13] Yujie Wu, Lei Deng, Guoqi Li, Jun Zhu, and Luping Shi, “Spatio-temporal backpropagation for training high-performance spiking neural networks,” *Frontiers in Neuroscience*, vol. 12, 2018.
- [14] Arnon Amir, Brian Taba, David Berg, Timothy Melano, Jeffrey McKinstry, Carmelo Di Nolfo, Tapan Nayak, Alexander Andreopoulos, Guillaume Garreau, Marcela Mendoza, Jeff Kusnitz, Michael Debole, Steve Esser, Tobi Delbrück, Myron Flickner, and Dharmendra Modha, “A low power, fully event-based gesture recognition system,” in *2017 IEEE Conference on Computer Vision and Pattern Recognition (CVPR)*, 2017, pp. 7388–7397.
- [15] Lang Feng, Qianhui Liu, Huajin Tang, De Ma, and Gang Pan, “Multi-level firing with spiking ds-resnet: Enabling better and deeper directly-trained spiking neural networks,” in *Proceedings of the Thirty-First International Joint Conference on Artificial Intelligence, IJCAI-22*, Lud De Raedt, Ed. 7 2022, pp. 2471–2477, International Joint Conferences on Artificial Intelligence Organization, Main Track.
- [16] Chaoteng Duan, Jianhao Ding, Shiyan Chen, Zhaofei Yu, and Tiejun Huang, “Temporal effective batch normalization in spiking neural networks,” *Advances in Neural Information Processing Systems*, vol. 35, pp. 34377–34390, 2022.
- [17] Hongmin Li, Hanchao Liu, Xiangyang Ji, Guoqi Li, and Luping Shi, “Cifar10-dvs: An event-stream dataset for object classification,” *Frontiers in Neuroscience*, vol. 11, 2017.
- [18] Garrick Orchard, Ajinkya Jayawant, Gregory K. Cohen, and Nitish Thakor, “Converting static image datasets to spiking neuromorphic datasets using saccades,” *Frontiers in Neuroscience*, vol. 9, 2015.
- [19] A. Krizhevsky and G. Hinton, “Learning multiple layers of features from tiny images,” *Handbook of Systemic Autoimmune Diseases*, vol. 1, no. 4, 2009.
- [20] Hao Li, Zheng Xu, Gavin Taylor, Christoph Studer, and Tom Goldstein, “Visualizing the loss landscape of neural nets,” in *Neural Information Processing Systems*, 2018.